Prediction of Group-IV Multiferroic Films with Giant Mid-infrared Responsivity

Shuxin Luo[1,#], Yongle Zhong[1,#], Yuxiang Xiao[1], Wentao Li[1], Songyu Chen[1], Jie Yang[3], Wen Xiong[4], Zhengfang Qian[1], and Pu Huang[1,2,*]

[1]State Key Laboratory of Radio Frequency Heterogeneous Integration, College of Physics and Optoelectronic Engineering, Shenzhen University, Shenzhen, 518060, China

[2]Key Laboratory of Optoelectronic Devices and Systems of Ministry of Education and Guangdong Province, College of Physics and Optoelectronic Engineering, Shenzhen University, Shenzhen. 518060. China

[3]Key Laboratory of Material Physics, School of Physics, Ministry of Education, Zhengzhou University, Zhengzhou 450001, China

[4]Chongqing Institute of Green and Intelligent Technology, Chinese Academy of Sciences, Chongqing, 400714, China

[#]These authors contributed equally to this work

[*]Email: arvin_huang@szu.edu.cn

Table of contents

Table S1 The little-group representation of the VB and CB states for Ge thin film with $Pmc2_1$ symmetry.

IRREP	E	$C_2(z)$	σ_v	σ_v'
A_1	1	1	1	1
A_2	1	1	-1	-1
B_1	1	-1	1	-1
B_2	1	-1	-1	1

[a]E denotes the identity operation.

[b]$C_2(z)$ represents a $180°$ rotation about the *z*-axis; σ_v and σ_v' are both vertical mirror planes that contains the *z*-axis and are parallel to the *xz*- and *yz*- planes, respectively.

[c]In the IRREP (irreducible representation) column, A and B denote one-dimensional irreducible representations that are symmetric (A) or antisymmetric (B) with respect to the principal rotation axis.

[d]The subscripts 1 and 2 further distinguish their behavior under the two mirror operations: 1 indicates even parity and 2 indicates odd parity. The values +1 and -1 in the table represent the characters of the corresponding symmetry operations in each irreducible representation: +1 indicates that the wavefunction remains in-phase under the operation, whereas -1 signifies a phase inversion. These character values facilitate the symmetry analysis of electric dipole transitions between different energy bands.

[e]For instance, the three Cartesian components of the electric dipole operator μ_i transform as $B_1(\mu_x)$, $B_2(\mu_y)$, and $A_2(\mu_z)$ under the $Pmc2_1$ space group. Accordingly, for *z*-polarized light absorption (corresponding to μ_z), the optical transition between two energy bands is symmetry-allowed only if the direct product $\Gamma_{final}\otimes\mu_z\otimes\Gamma_{initial}$ contains the totally symmetric irreducible representation A_1. If A_1 is not contained in this product, the transition is symmetry-forbidden.

Table S2 Elastic modulus C ($\mathrm{Jm^{-1}}$) and deformation potential E (eV) at 300 K for Ge thin films with $Pmc2_1$ symmetry.

Thickness	C_e^x	C_e^y	C_h^x	C_h^y	E_e^x	E_e^y	E_h^x	E_h^y
1L	68.96	44.38	68.96	44.38	4.46	0.85	8.45	1.36
2L	150.7	143.1	150.7	143.1	0.87	3.47	0.007	2.08
3L	221.2	228.6	221.2	228.6	1.20	4.19	0.37	1.93
4L	299.6	319.4	299.6	319.4	1.26	5.12	1.66	3.66
5L	383.9	421.5	383.9	421.5	1.78	4.21	2.47	2.97

Table S3 Curvature decomposition and dominant CB_1–VB_1 interband coupling metrics along Γ–X direction for Ge thin films.

Thickness	E''_{tot}	E''_{intra}	E''_{inter}	$E''_{CB1\leftarrow VB1}$	$\left\|V_{CB1,VB1}\right\|^2$	$\Delta E_{CB1,VB1}$
1L	43.33	-7.38	50.71	5.75	1.57	0.55
2L	111.67	-9.79	121.46	93.23	21.12	0.45
3L	238.84	-18.24	257.07	241.79	43.27	0.36
4L	338.97	-19.05	358.01	342.29	52.35	0.31
5L	416.22	-22.62	438.83	422.49	57.04	0.27

[a] $E''_{tot} = \partial^2 E/\partial k_x^2 = E''_{intra} + E''_{inter}$, denotes the total band curvature evaluated along Γ–X, in units of $\mathrm{eV}\cdot\mathrm{Å}^2$.

[b] $E''_{intra} = \langle n|\partial_x^2 H|n\rangle$ and $E''_{inter} = 2\sum_{m\neq n}|\langle n|\partial_x H|m\rangle|^2/(E_n - E_m)$, where n is CB_1.

[c] $E''_{\mathrm{CB1}\leftarrow\mathrm{VB1}}$ denotes the VB_1 contribution to the interband curvature of CB_1, in units of $\mathrm{eV}\cdot\mathrm{Å}^2$.

[d] $\left|V_{\mathrm{CB1,VB1}}\right|^2 = |\langle CB1|\partial_x H|VB1\rangle|^2$ is the numerator of the CB_1–VB_1 interband coupling term, in units of $(\mathrm{eV}\cdot\mathrm{Å})^2$.

[e] $\Delta E_{\mathrm{CB1,VB1}} = E_{CB1} - E_{VB1}$, in units of eV.

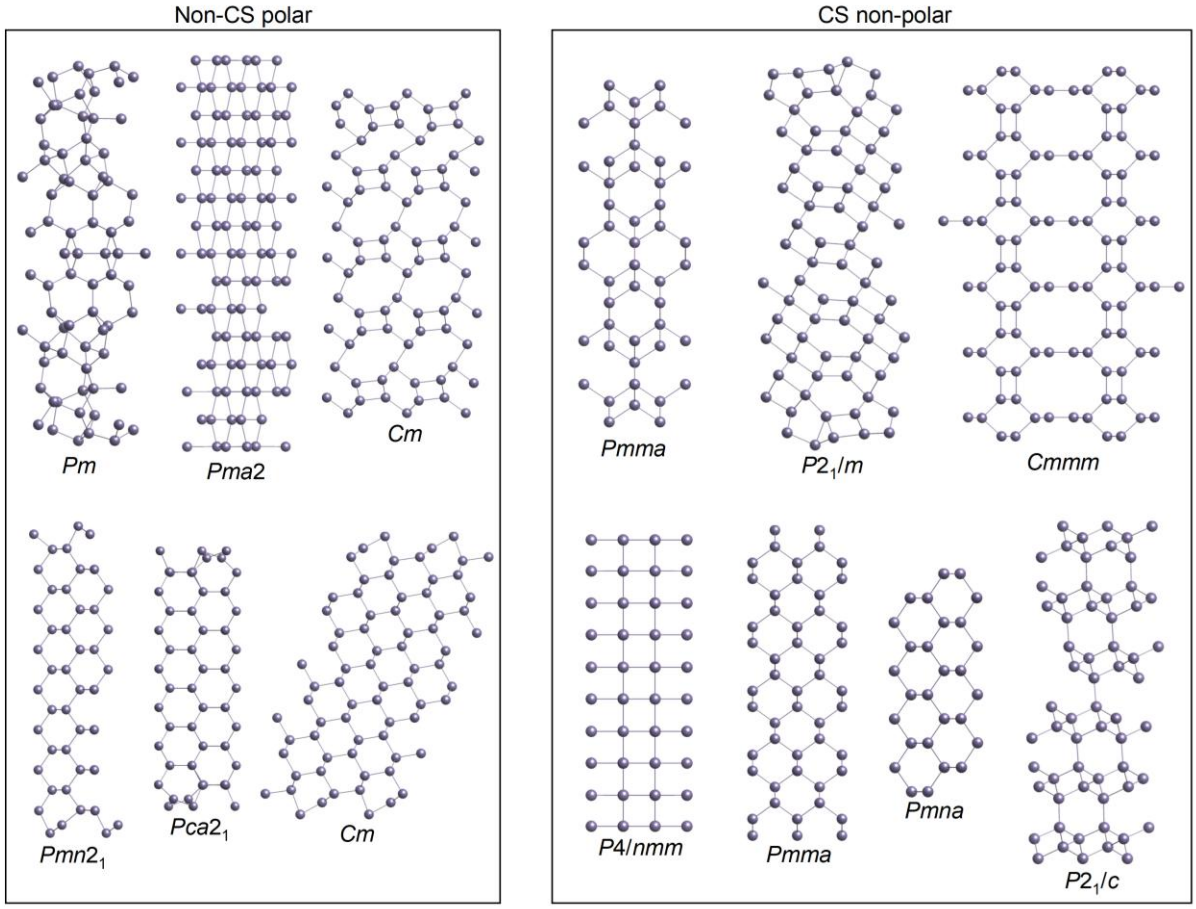

Fig. S1 Additional 13 phases for group-IV thin films identified from AIMD-based film-phase exploration framework, including six FE phases and seven CS phases.

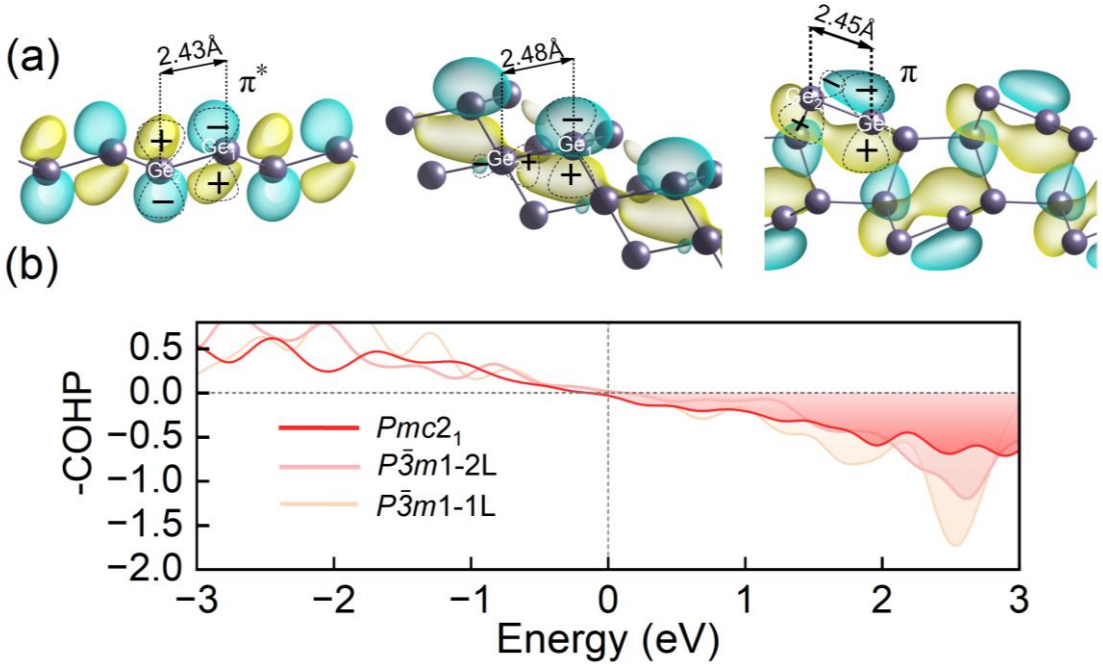

Fig. S2 (a) Evolution of orbital interactions under the reconstruction process. (b) -COHP curves for the above three structures, with the antibonding peak of the $Pmc2_1$ FE phase significantly weakened (the ICOHP values at conduction band are 1.13, 1.20 and 1.68 eV for $Pmc2_1$, $P\bar{3}m1$-1L and $P\bar{3}m1$-2L, respectively).

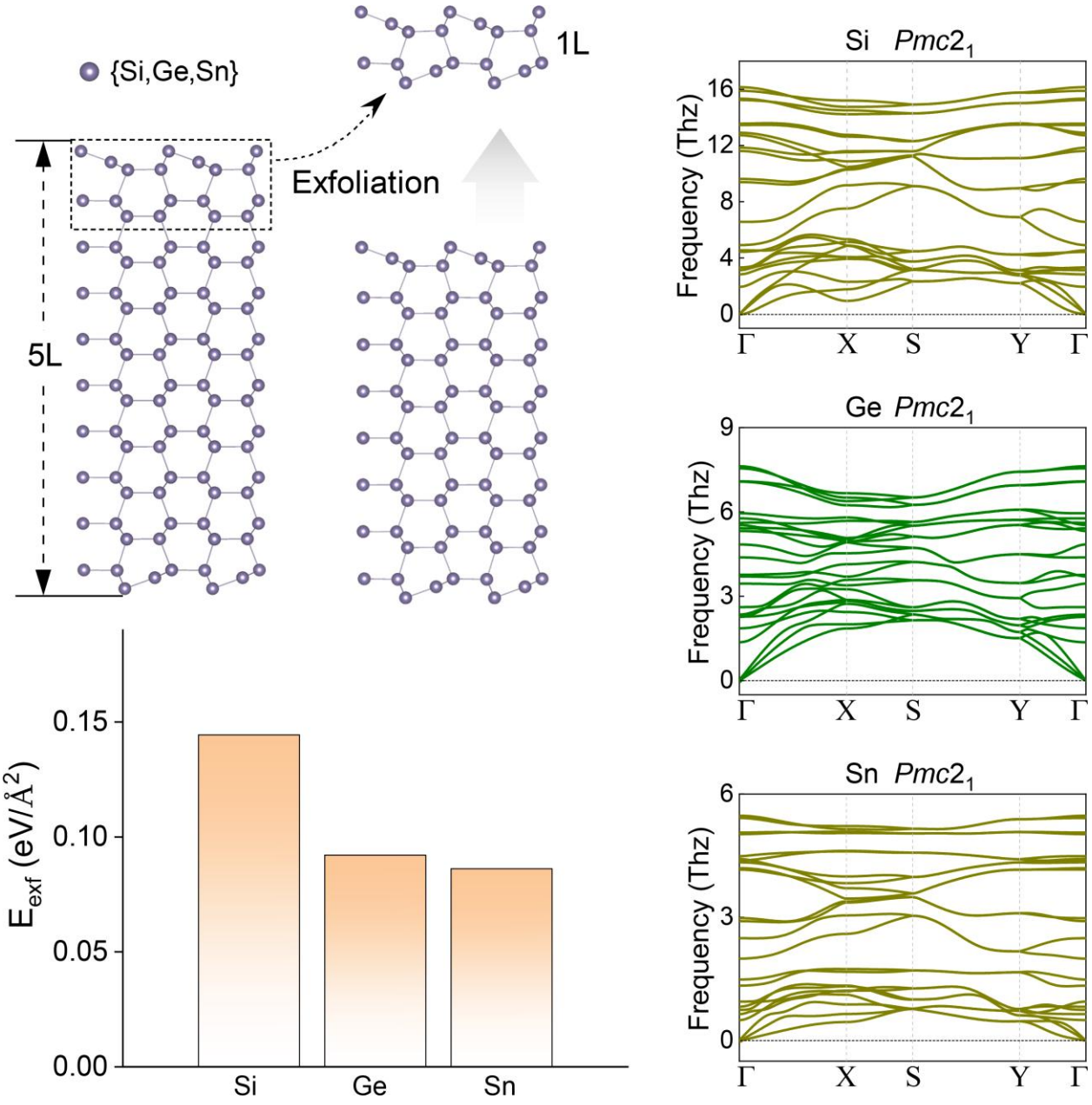

Fig. S3 Left: Exfoliation energies of isolating group-IV monolayers from thin films. Right: Phonon spectra for the group-IV monolayers with $Pmc2_1$ symmetry.

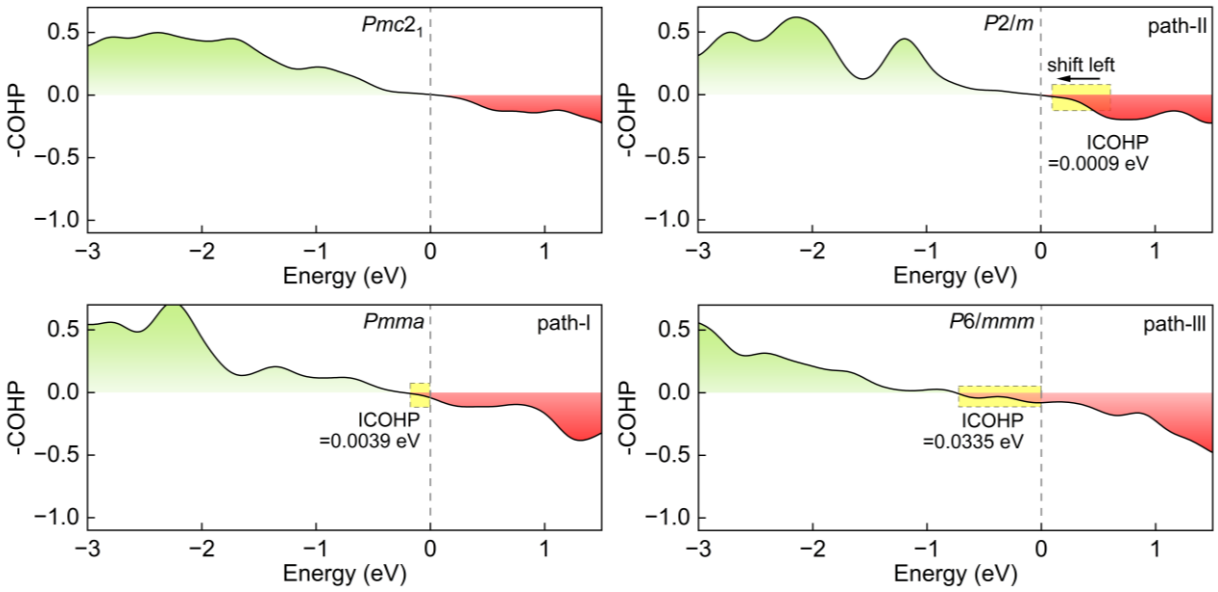

Fig. S4 -COHP curve variations at the highest barrier points of the three distinct phase transition pathways for 1L Ge thin film.

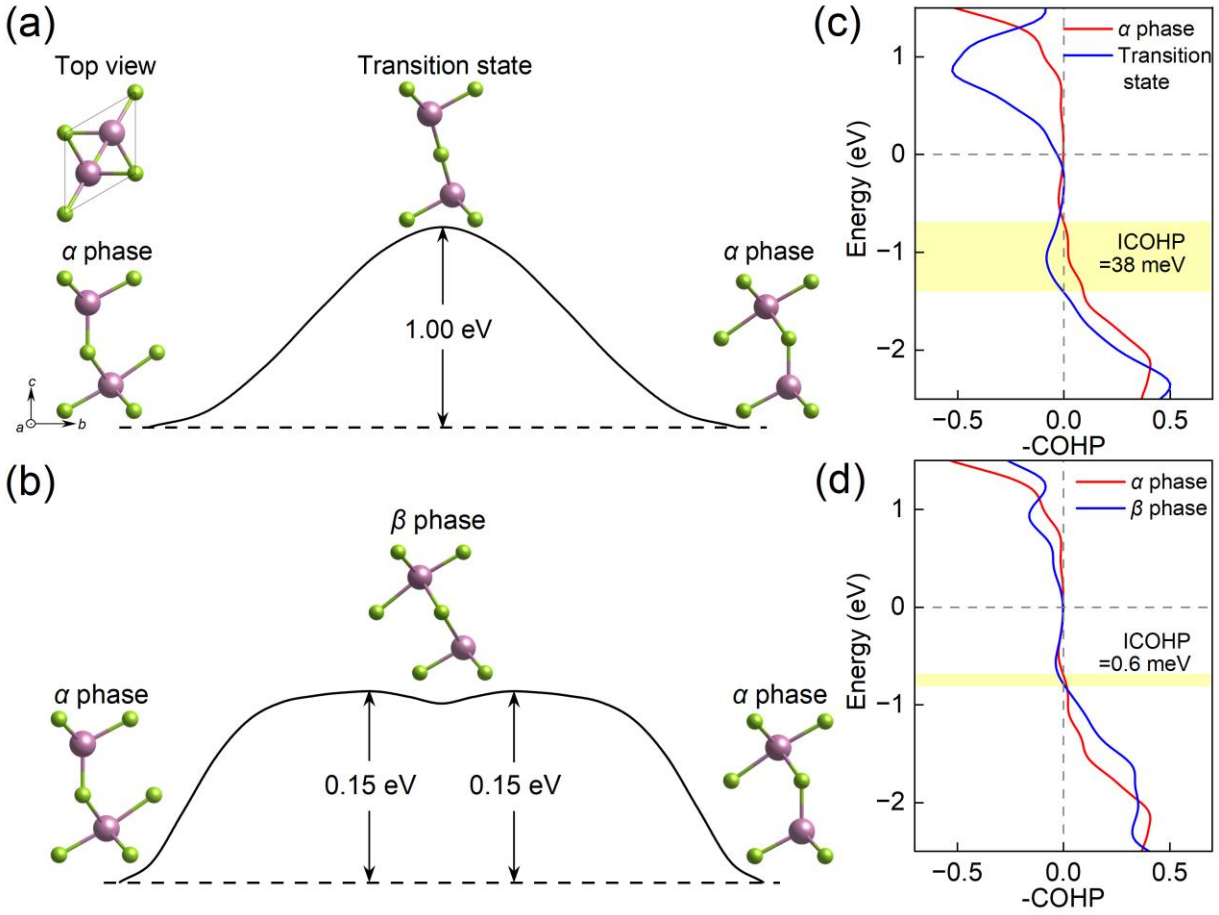

Fig. S5 (a, b) Two phase transition pathways of In_2Se_3 with markedly different activation barriers. (c, d) Comparison of the -COHP curves between the initial phases and the structures at the highest barrier points along each transition pathway, indicating the subtle changes in antibonding interactions for the low-barrier transition pathway.

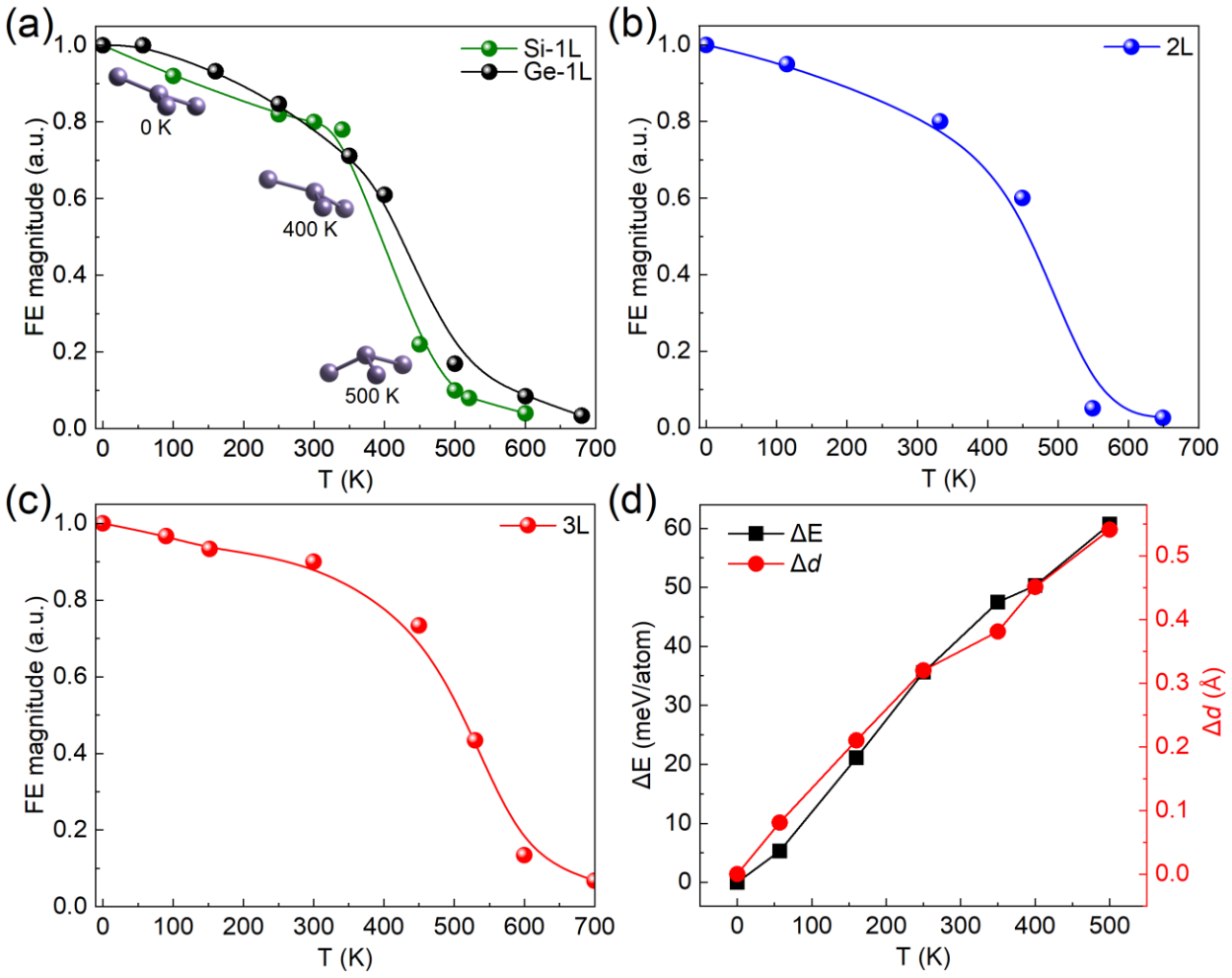

Fig. S6 (a-c) Temperature-dependent changes in the magnitude of FE polarization for Si and Ge thin films with $Pmc2_1$ symmetry. (d) Variation in energy and out-of-plane displacement of the central atom in the planar-triangular motif of Ge as a function of temperature.

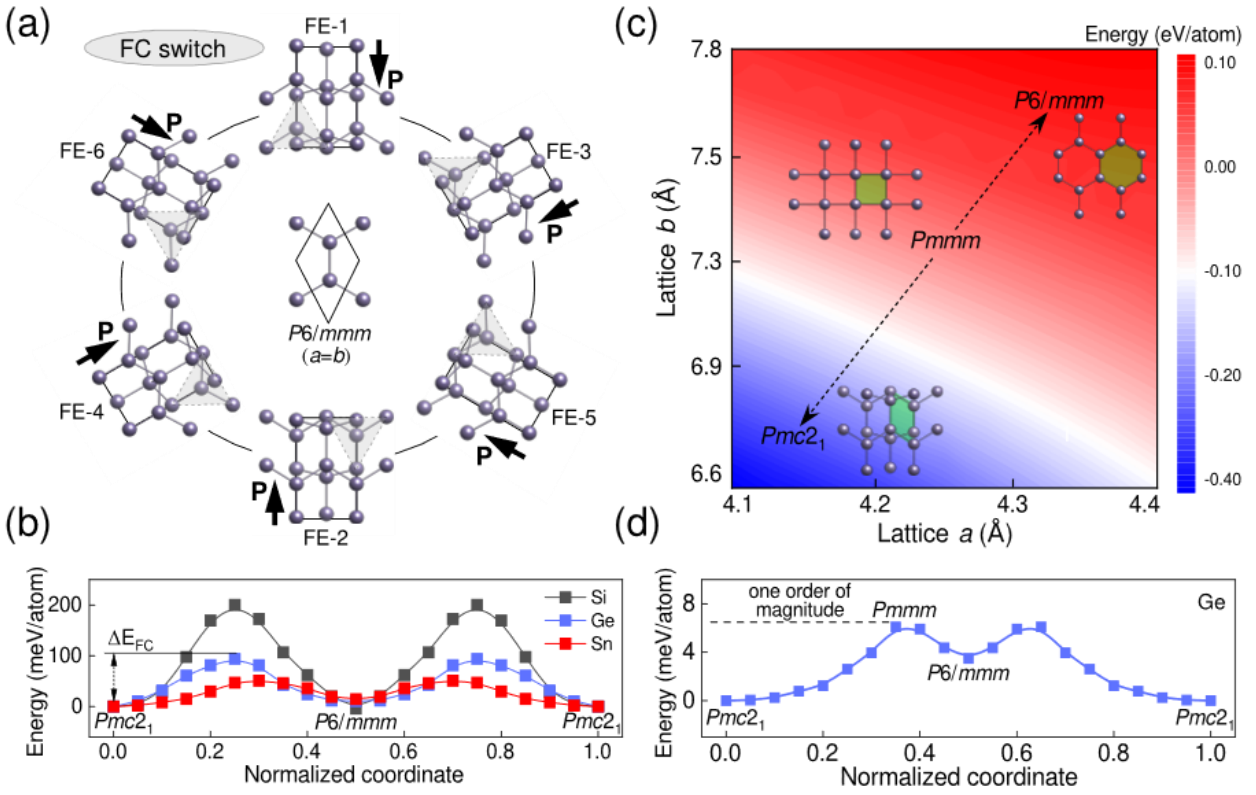

Fig. S7 (a) FC phase transition for the 1L Ge, where in-plane atomic displacements and π/3 rotations of tetrahedral and triangular motifs reorient the FE polarization, yielding six distinct FE phases. (b) FC phase transition barrier ($Pmc2_1 \leftrightarrow P6/mmm$) for the group-IV monolayers. (c) Lattice deformation strategy that captures a $Pmmm$ transient state with reduced barrier energy. (d) Substantially lowered barrier energy for the transient-state-mediated FC transition pathway ($Pmc2_1 \rightarrow Pmmm \rightarrow P6/mmm$) in the 1L Ge.

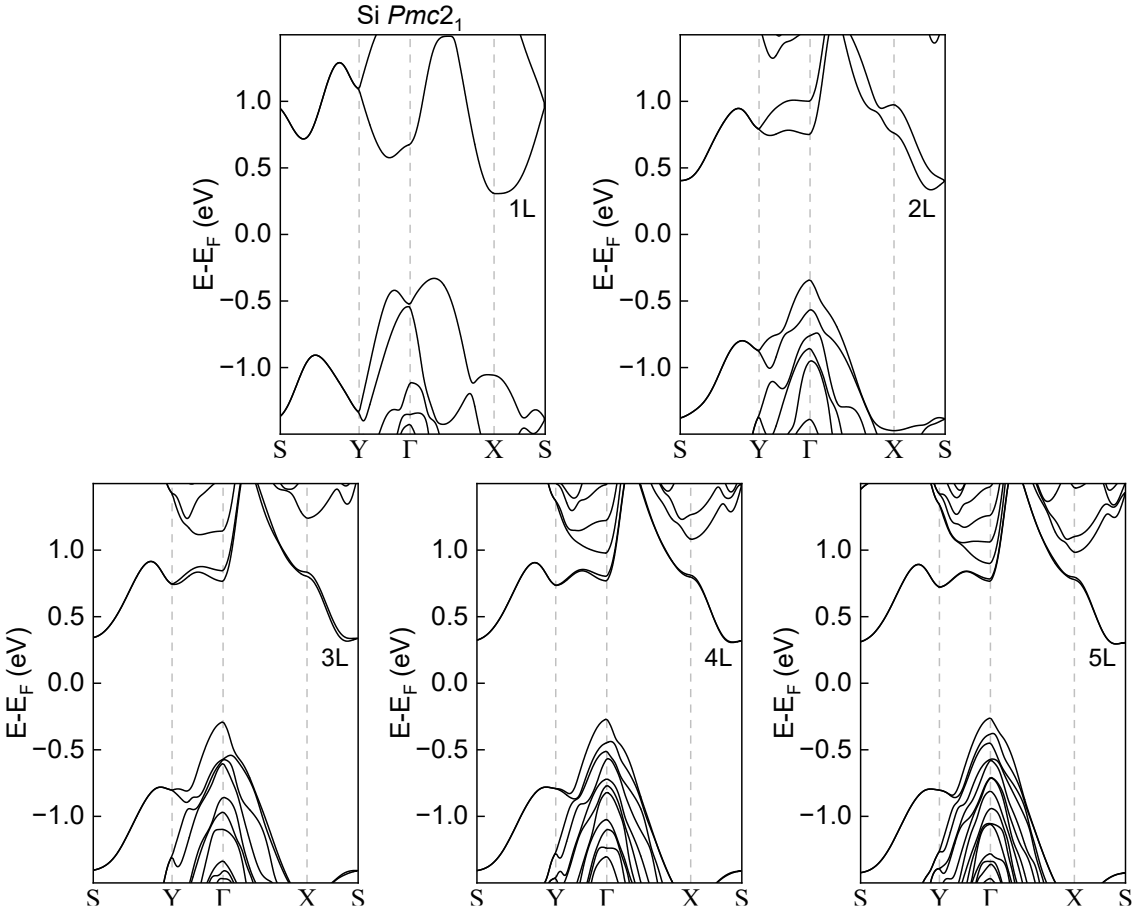

Fig. S8 Electronic band structures (HSE06) for Si thin films with $Pmc2_1$ symmetry.

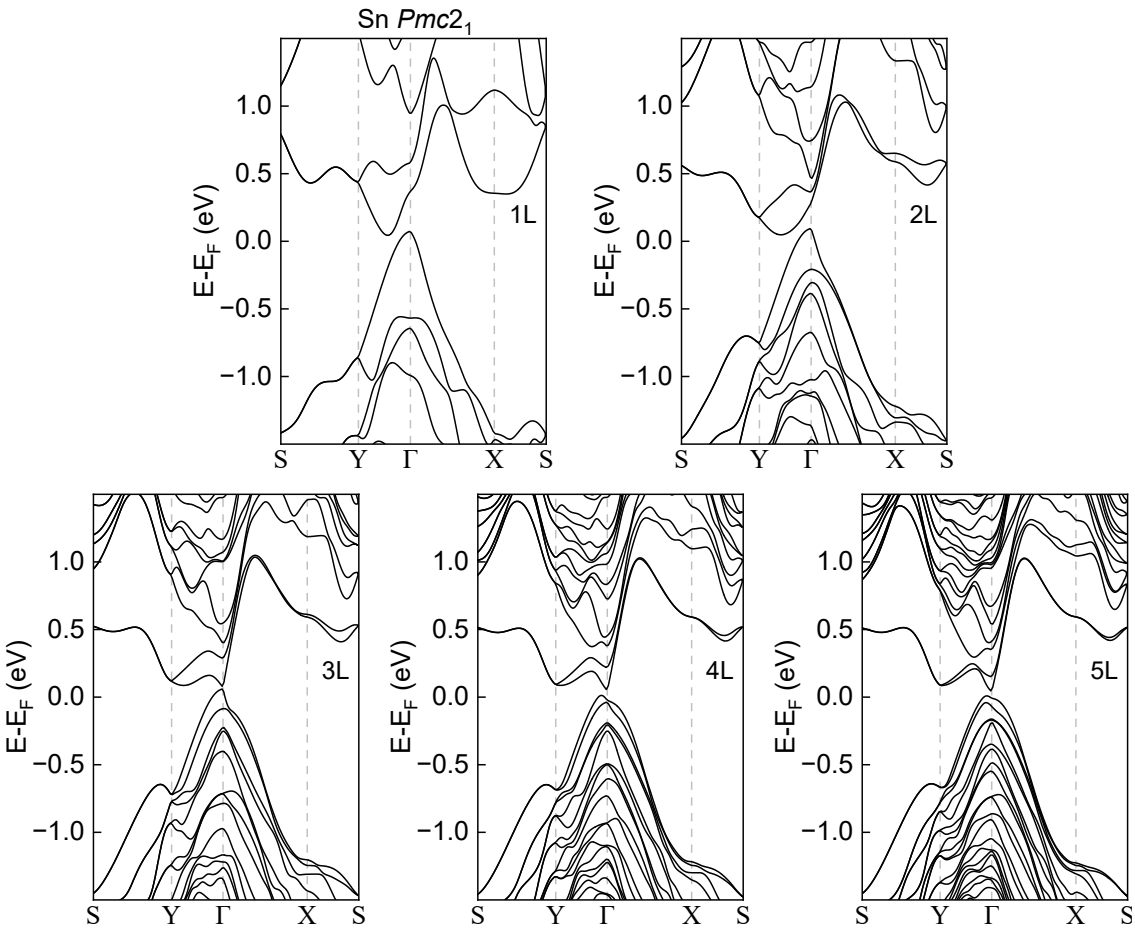

Fig. S9 Electronic band structures (HSE06) for Sn thin films with $Pmc2_1$ symmetry.

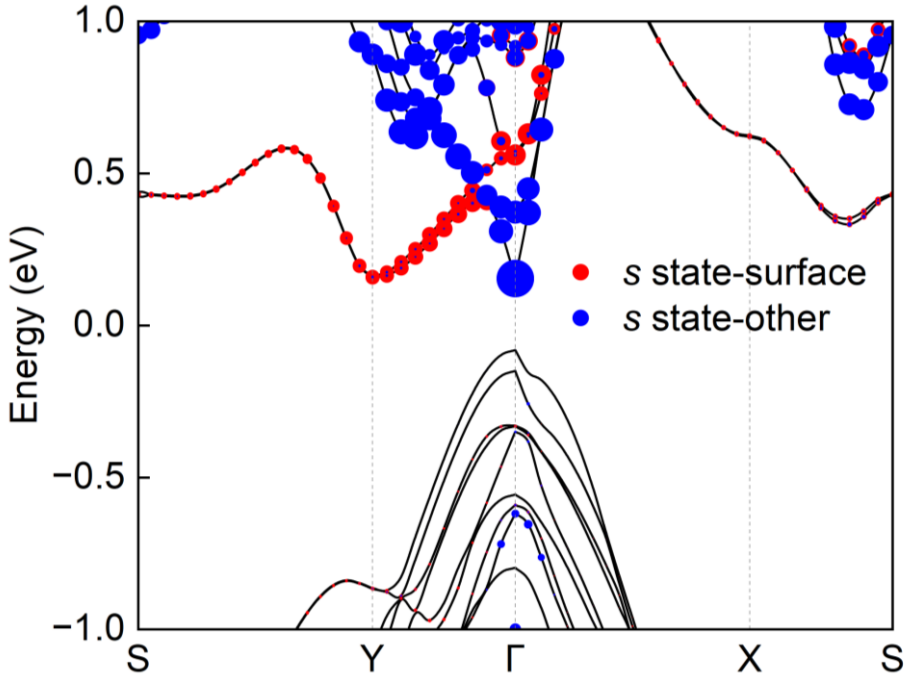

Fig. S10 PDOS band structure for the ~3.3 nm Ge thin film, indicating the enhanced *s* state contribution from the interior Ge atoms to the steep conduction band.

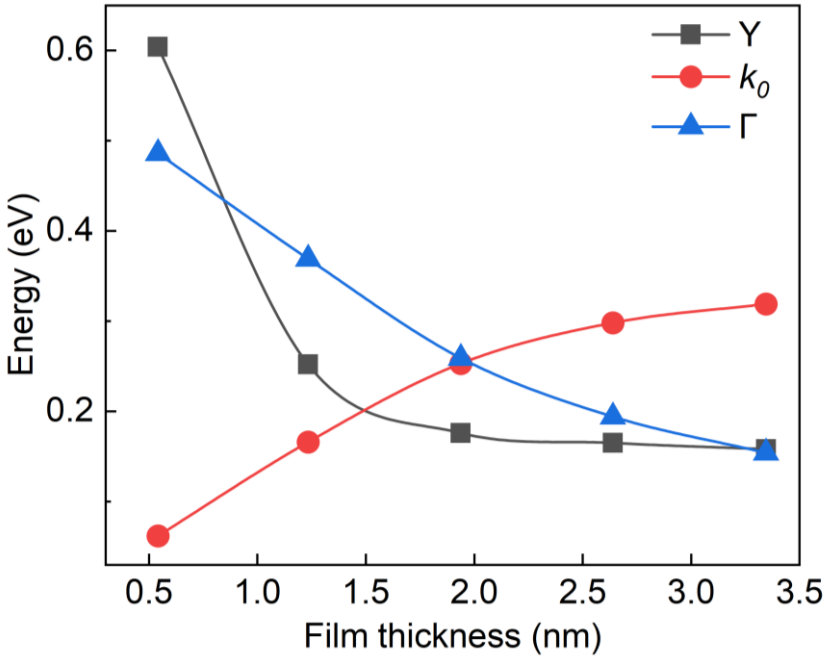

Fig. S11 Evolution of the CB_1 band structure with increasing Ge thin film thickness, showing the energy shifts at the Y point, k_0, and the Γ point. Here, k_0 represents the CB minimum wave vector of CB_1 band in 1L Ge.

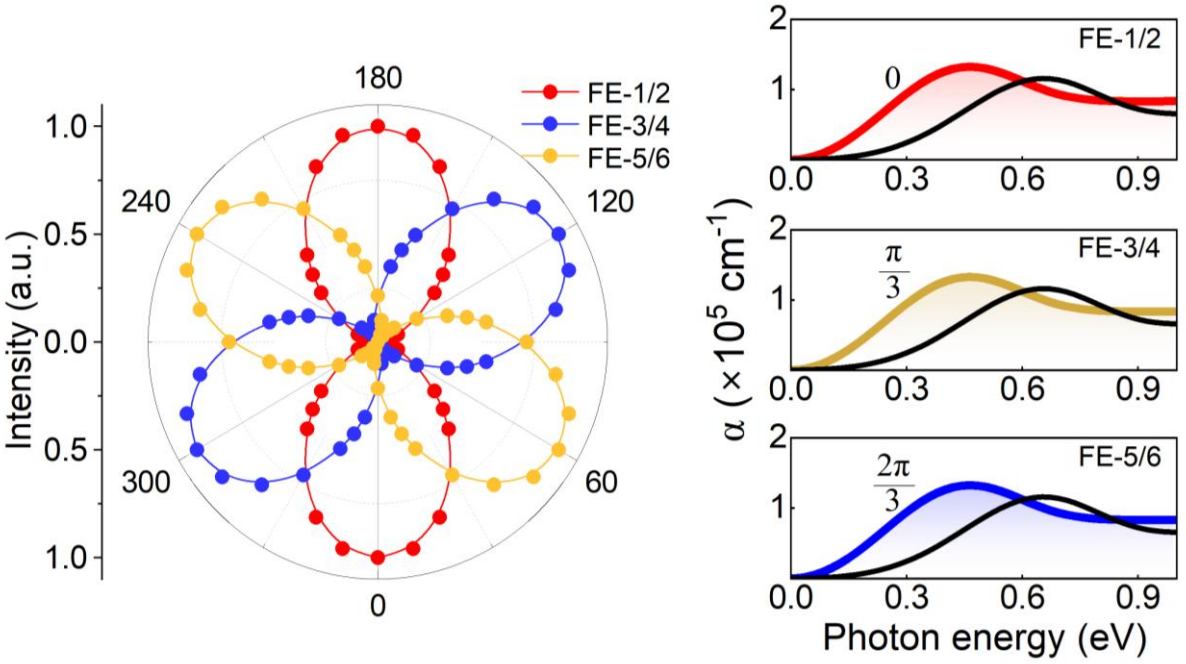

Fig. S12 Switchable in-plane polarization-dependent absorption for Ge thin film. The left panel shows the angular dependence of absorption intensity for three pairs of FE variants (FE-1/2, FE-3/4 and FE-5/6), whose principal absorption directions rotate by π/3 in the 2D plane. The right panels present the corresponding absorption spectra for selected polarization angles.

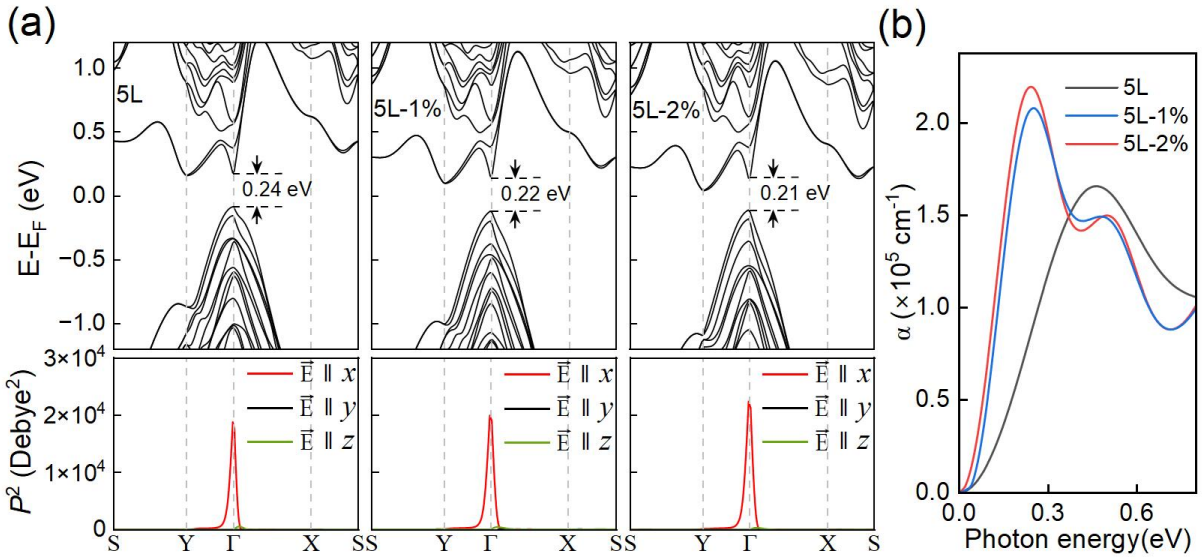

Fig. S13 Band structures and TDM for Ge thin films with 0-2% compressive strain along the *a*-axis. (b) Absorption spectra of Ge thin films, illustrating the enhancement in absorption as the compressive strain increases from 0% to 2%.

Methods

Refined AIMD workflow

To accurately capture emerging structural phases during the search process, it is essential to carefully select the tolerance parameter $\boldsymbol{\delta}$ in the structural matching criterion. An overly stringent tolerance can hinder the identification of genuine structural transitions, potentially trapping the system in saddle-like regions on the potential-energy surface. We employ a refined *ab* initio molecular dynamics (AIMD) approach for phase exploration. To enhance exploration beyond energy barriers, we intentionally increase the magnitude of structural perturbations, quantified by the step-to-step atomic displacement ΔR. When the atomic displacements between consecutive steps are too small, the system tends to relax back to its initial configuration, remaining confined to local minima. To mitigate this, we increase the ionic time step, which amplifies atomic displacements between successive AIMD steps, facilitating the traversal of energy barriers and enabling access to new regions of the energy landscape. Ionic forces at each time step are evaluated using density functional theory (DFT), ensuring a precise description of interatomic interactions along the trajectory. Representative configurations sampled from high-energy, saddle-like regions are extracted and subsequently optimized through DFT. Prior to optimization, symmetry operations are applied to symmetrize the snapshots, ensuring that the relaxed structures conform to candidate space groups. The space group of each relaxed structure is then determined using symmetry-operation analysis based on group theory. In parallel, we quantify the local bonding and

coordination motifs for every AIMD snapshot using the CrystalNN near-neighbor algorithm [1] and the associated local structure order parameters (LSOPs) implemented in pymatgen [2].

For each atom a at snapshot i, we evaluate the local structure order parameters $q_m(a,i) \in [0,1]$ for target motifs m, including tetrahedral, trigonal-planar/pyramidal, and octahedral configurations, as well as additional motifs such as square-planar and trigonal-bipyramidal. The LSOPs measure the similarity between the first-shell neighbor geometry and an ideal motif template. This analysis accounts for variations in local coordinate systems (permutations), selecting the maximum resemblance

$$q_m(a,i) = \max_j \{q_{m,j}(a,i)\} \tag{1}$$

Here, $q_{m,j}$ is calculated by choosing a neighbor atom j as a tentative "north pole" to construct a local spherical coordinate system. Deviations from the ideal angular positions are penalized using cosine terms and Gaussian kernels. Each atom is then assigned a discrete motif label $\mathcal{M}_a^{(i)}$ based on a threshold τ (set to 0.8 in our workflow). The assignment follows the criteria

$$\mathcal{M}_a^{(i)} = \begin{cases} \arg\max_{m \in \mathcal{S}} q_m(a,i), & \text{if } \max_{m \in \mathcal{S}} q_m(a,i) \geq \tau \\ \text{other/undefined}, & \text{otherwise} \end{cases} \tag{2}$$

To distinguish between tetrahedral and defective-tetrahedral motifs, we combine the tetrahedral LSOP and the instantaneous coordination number

$$\text{tetrahedral:} \quad q_{\text{tet}}(a,i) \geq \tau \ \wedge \ \text{CN}_a^{(i)} \approx 4 \tag{3}$$

$$\text{defective-tetrahedral:} \quad q_{\text{tet}}(a,i) \geq \tau \ \wedge \ \text{CN}_a^{(i)} \approx 3 \tag{4}$$

Similarly, trigonal and octahedral motifs are identified based on their respective LSOP values and characteristic coordination numbers

$$\text{trigonal: } \max\left(q_{\text{tri}_{\text{plan}}}, q_{\text{tri}_{\text{pyr}}}\right) \geq \tau \ \wedge \ \text{CN} \approx 3 \ (4) \tag{5}$$

$$\text{octahedral: } q_{\text{oct}}(a,i) \geq \tau \ \wedge \ \text{CN} \approx 6 \tag{6}$$

Motif interconversion events are recorded whenever an atom's motif label changes between consecutive snapshots

$$\Delta\mathcal{M}_a^{(i\to i+1)} = \begin{cases} 1, & \text{if } \mathcal{M}_a^{(i)} \neq \mathcal{M}_a^{(i+1)} \\ 0, & \text{otherwise.} \end{cases} \tag{7}$$

Additionally, we track the motif population fractions at each time step

$$p_m(i) = \frac{1}{N}\sum_{a=1}^{N}\left[\mathcal{M}_a^{(i)} = m\right] \tag{8}$$

These population fractions provide a compact trajectory-level fingerprint for detecting local rehybridization and coordination rearrangements that occur concurrently with symmetry changes.

Electronic structure calculation

The DFT calculations were performed using the projector augmented wave (PAW) method, as implemented in the Vienna Ab initio Simulation Package (VASP) [3]. Exchange–correlation interactions were treated with the Perdew-Burke-Ernzerhof (PBE) functional within the generalized gradient approximation (GGA) [4]. A plane-wave energy cutoff of 520 eV was employed for all calculations. The Brillouin zone was sampled using a Γ-centered k-point grid with a uniform reciprocal-space spacing of 0.02 Å^{-1}, ensuring convergence for both structural relaxations and electronic-structure evaluations. The total energy convergence criterion was set to 10^{-7} eV, and the atomic coordinates and lattice vectors were fully relaxed until the residual Hellmann-Feynman forces on all atoms were smaller than 10^{-3} eV Å^{-1}. A vacuum layer of

approximately 15 Å was introduced along the out-of-plane direction to prevent spurious interlayer interactions. The Heyd-Scuseria-Ernzerhof hybrid functional (HSE06) was adopted for accurate band-structure calculations [5,6]. Polarization-resolved optical properties were computed within the independent-particle approximation by evaluating the real and imaginary components of the dielectric tensor and subsequently deriving the polarization-dependent absorption coefficient. The phase transition barriers were evaluated by the solid-state nudged elastic band (SS-NEB) method [7], allowing for careful tracking of symmetry evolution along each intermediate image. Phonon spectra were computed *via* the finite-displacement approach implemented in the PHONOPY code [8].

FE polarization evaluation

The FE polarization was quantified *via* the Born effective charge (BEC) method, with finite atomic displacements along the polarization-switching pathway according to $P = \frac{e}{S}\sum_i (Z_i^* \cdot \Delta u_i)$, where S is the unit-cell area, Z_i^* is the BEC tensor of atom i along the FE transition path, and Δu_i denotes its displacement vector. Finite-temperature structural fluctuations were sampled by AIMD in the canonical (NVT) ensemble using VASP. A time step of 3 fs and a total of 5000 MD steps were used. Statistically independent snapshots were extracted from equilibrated trajectories and post-processed using single-point calculations analyzed with LOBSTER to obtain Löwdin partial charges [9]. The charge on atom A was calculated by

$$q_A = N_A - \sum_{\mu \in A} \mathrm{GP}_\mu \tag{9}$$

where N_A is the number of valence electrons and GP_μ is the gross orbital population derived from the density-matrix formalism. These environment-dependent charges were then used to estimate the instantaneous polarization at temperature T within a charge-partitioning dipole model

$$\mathbf{P}(T) = \frac{1}{V_{\mathrm{uc}}} \sum_A q_A(T)\, \mathbf{r}_A(T) \tag{10}$$

where V_{uc} is the unit-cell volume and $\mathbf{r}_A(T)$ is the atomic position in the corresponding snapshot. For each snapshot, $\mathbf{P}(T)$ was projected onto the zero-temperature FE polarization direction $\mathbf{e}_0$, yielding $P_T(T) = \mathbf{P}(T) \cdot \mathbf{e}_0$. The retention of FE order was quantified by normalizing $P_T(T)$ to the 0 K reference polarization P_0 of the fully relaxed FE ground state, defining a dimensionless order parameter

$$\tilde{P}(T) = \frac{P_T(T)}{P_0} = \frac{\mathbf{P}(T) \cdot \mathbf{e}_0}{P_0} \tag{11}$$

This charge-based $\tilde{P}(T)$ was used to construct polarization–temperature curves and serves as an effective order parameter for the thermally driven evolution of the FE distortion.

Photocurrent calculation

Lateral p–n junction devices were constructed to model Ge thin-film photodetectors, using a representative sheet doping density of 4×10^{12} cm^{-2} in the source and drain. Ground-state electronic structures were obtained with the PBE+GGA-1/2 exchange–correlation functional [10], which reproduces the band structure from HSE06 [5,6], and transport calculations were performed at 300 K. The periodic, Neumann, and Dirichlet boundary conditions were applied along the *x*, *y*,

and z directions, respectively. Photocurrent spectra were evaluated within the non-equilibrium Green's function (NEGF) method, accounting for single-photon absorption, as implemented in the QuantumATK 2021 package [11,12]. The photocurrent collected at electrode α is given by

$$I_\alpha = \frac{e}{\hbar}\int_{-\infty}^{+\infty}\sum_{\beta=L,R}[1-f_\alpha(E)]\,f_\beta(E-\hbar\omega)T^-_{\alpha,\beta}(\mathrm{E}) - f_\alpha(E)\big[1-f_\beta(E+\hbar\omega)\big]T^+_{\alpha,\beta}(E)dE \quad (12)$$

where $f_\alpha(E)$ is the Fermi distribution function of electrode α (α, β=L, R), e is the charge of an electron, and $\hbar$ is the reduced Planck constant. The first and second terms represent transport from electrode β to α and the reverse process, respectively, both including single-photon absorption. $T^{\pm}_{\alpha,\beta}$ is the transmission coefficient with the absorption of a single photon calculated by [13]

$$T^-_{\alpha,\beta}(E) = N\,Tr\big[M^+\tilde{A}_\alpha(E)MA_\beta(E-\hbar\omega)\big] \quad (13)$$

$$N\,T^+_{\alpha,\beta}(E) = N\,Tr\big[M\tilde{A}_\alpha(E)M^+A_\beta(E+\hbar\omega)\big] \quad (14)$$

where N is the photon number, M is the transition matrix describing photon absorption, and A_α is the spectral function defined as $A_\alpha = G\Gamma_\alpha G^+$, with G and Γ_α being the Green function and broadening function, respectively.

Second-order perturbative $\mathbf{k}\cdot\mathbf{p}$ band curvature calculation

In tight-binding (TB) notation, one has

$$H(\boldsymbol{k}) = \sum_{\boldsymbol{R}} H(\boldsymbol{R})e^{i\boldsymbol{k}\cdot\boldsymbol{R}} \quad (15)$$

Performing a Taylor (harmonic) expansion around the Γ point gives

$$H(\boldsymbol{k}) = H_0 + \sum_{\boldsymbol{\alpha}} k_\alpha H_\alpha + \frac{1}{2}\sum_{\boldsymbol{\alpha},\boldsymbol{\beta}} k_\alpha k_\beta H_{\alpha,\beta} + \cdots high\ order \quad (16)$$

The first-order term is

$$H_\alpha = \frac{\partial H}{\partial k_\alpha}\Big|_\Gamma = \sum_R R_\alpha H(\boldsymbol{R}) \tag{17}$$

The second-order term is

$$H_{\alpha,\beta} = \frac{\partial^2 H}{\partial k_\alpha \partial k_\beta}\Big|_\Gamma = -\sum_{\boldsymbol{R}} R_\alpha R_\beta H(\boldsymbol{R}) \tag{18}$$

As $H(\mathbf{R})$ is a Hermitian matrix, it satisfies the eigenvalue equation

$$H(\boldsymbol{R})|n\rangle = E(\boldsymbol{R})|n\rangle \tag{19}$$

Here, we choose the normalization

$$\langle n|n\rangle = 1 \tag{20}$$

Taking the first derivative of the eigenvalue equation and applying the Hellmann–Feynman theorem gives

$$E'(\boldsymbol{R}) = \langle n|H'(\boldsymbol{R})|n\rangle \tag{21}$$

Rearranging the first-derivative equation results in

$$\big(H(\boldsymbol{R}) - E(\boldsymbol{R})\big)|n'\rangle = -(H'(\boldsymbol{R}) - E'(\boldsymbol{R}))|n\rangle \tag{22}$$

Introduce a complete orthonormal basis $\{|m\rangle\}$ of $H(\boldsymbol{R})$, and expand

$$|n'\rangle = \sum\nolimits_m |m\rangle\langle m|\, n'\rangle \tag{23}$$

This leads to

$$\langle m\big|\big(H(\boldsymbol{R}) - E(\boldsymbol{R})\big)\big|n'\rangle = \big(E_m(\boldsymbol{R}) - E_n(\boldsymbol{R})\big)\langle m|n'\rangle = -\langle m|H'(\boldsymbol{R})|n\rangle + E'(\boldsymbol{R})\langle m|n\rangle \tag{24}$$

$$(E_m(\boldsymbol{R}) - E_n(\boldsymbol{R}))\langle m|n'\rangle = -\langle m|H'(\boldsymbol{R})|n\rangle \tag{25}$$

$$\langle m|n'\rangle = \frac{\langle m|H'(\boldsymbol{R})|n\rangle}{E_n(\boldsymbol{R}) - E_m(\boldsymbol{R})} \tag{26}$$

Consequently, the total energy second derivative is

$$E''_{\mathrm{tot}} = \langle n'|H'(\boldsymbol{R})|n\rangle + \langle n|H''(\boldsymbol{R})|n\rangle + \langle n|H'(\boldsymbol{R})|n'\rangle \tag{27}$$

By utilizing Hermiticity, we obtain

$$\langle n'|H'(\boldsymbol{R})|n\rangle + \langle n|H'(\boldsymbol{R})|n'\rangle = 2Re\langle n|H'(\boldsymbol{R})|n'\rangle \tag{28}$$

The interband coupling term becomes

$$\langle n|H'(\boldsymbol{R})|n'\rangle = \sum_{m\neq n}\langle n|H'(\boldsymbol{R})|m\rangle\langle m|n'\rangle = \sum_{m\neq n}\langle n|H'(\boldsymbol{R})|m\rangle\frac{\langle m|H'(\boldsymbol{R})|n\rangle}{E_n(\boldsymbol{R}) - E_m(\boldsymbol{R})} \tag{29}$$

Hence, the total second-order energy derivative is

$$E''_{\mathrm{tot}} = \langle n|H''(\boldsymbol{R})|n\rangle + 2\sum_{m\neq n}\langle n|H'(\boldsymbol{R})|m\rangle\frac{\langle m|H'(\boldsymbol{R})|n\rangle}{E_n(\boldsymbol{R}) - E_m(\boldsymbol{R})} \tag{30}$$

Thus, the curvature of band n is obtained from the second-order perturbative $\mathbf{k}\cdot\mathbf{p}$ structure

$$C_{\alpha,\beta} = \langle n|H_{\alpha,\beta}|n\rangle + 2\sum_{m\neq n}\frac{\langle n|H_\alpha|m\rangle\langle m|H_\beta|n\rangle}{E_n - E_m} \tag{31}$$

Band dispersion and curvature analysis

To understand the band dispersion of the band near the Γ point, we evaluate the band curvature tensor $C_{\alpha,\beta}$. A larger value of $|C_{\alpha,\beta}|$ (or a larger principal curvature) corresponds to a more pronounced, cusp-like dispersion near Γ. This can be related to the inverse effective-mass tensor, $(m^{*-1})_{\alpha,\beta} = C_{\alpha,\beta}/\hbar^2$. Therefore, the observation of a steep band can be quantitatively diagnosed by calculating $C_{\alpha,\beta}$ and analyzing its contributions. We calculate $C_{\alpha,\beta}$ directly from the real-space tight-binding Hamiltonian output by Wannier90 [14], which provides the matrix elements $H_{ij}(\boldsymbol{R})$ in the orthonormal Wannier basis $\{|i\rangle\}$, along with degeneracy weights $d_{\boldsymbol{R}}$ for each

lattice translation $\boldsymbol{R} = n_1\boldsymbol{a}_1 + n_2\boldsymbol{a}_2 + n_3\boldsymbol{a}_3$. Using these matrix elements, we reconstruct the Bloch Hamiltonian

$$H(\boldsymbol{k}) = \sum_{\boldsymbol{R}} \frac{H(\boldsymbol{R})}{d_{\boldsymbol{R}}}\, e^{i\boldsymbol{k}\cdot\boldsymbol{R}} \tag{32}$$

We then obtain its derivatives at the Γ point analytically within the Wannier representation

$$H_\alpha = \frac{\partial H}{\partial k_\alpha}\,|_\Gamma = i \sum_{\boldsymbol{R}} \frac{R_\alpha\, H(\boldsymbol{R})}{d_{\boldsymbol{R}}}, \qquad H_{\alpha,\beta} = \frac{\partial^2 H}{\partial k_\alpha \partial k_\beta}\,|_\Gamma = -\sum_{\boldsymbol{R}} \frac{R_\alpha R_\beta\, H(\boldsymbol{R})}{d_{\boldsymbol{R}}} \tag{33}$$

where R_α denotes the α-component of $\boldsymbol{R}$ in the chosen coordinate system to ensure the correct dimensionality of the curvature. Next, we diagonalize $H(\Gamma)$ to obtain the eigenvalues and eigenvectors within the Wannier subspace

$$H(\Gamma)|n\rangle = E_n|n\rangle, \qquad |n\rangle = \sum_i U_{in}\,|i\rangle \tag{34}$$

We calculate the matrix elements by transforming H_α and $H_{\alpha,\beta}$ into the band-eigenstate representation

$$\langle n|H_{\alpha,\beta}|n\rangle = (U^\dagger H_{\alpha,\beta} U)_{nn}, \qquad \langle n|H_\alpha|m\rangle = (U^\dagger H_\alpha U)_{nm} \tag{35}$$

By substituting these values into the expression for $C_{\alpha,\beta}$, we obtain a numerically stable and physically transparent decomposition of the Γ-point curvature, which is separated into intraband and interband coupling contributions. This decomposition allows us to identify whether the

observed steep band dispersion near Γ is driven by changes in the real-space hopping terms or by enhanced interband mixing due to larger velocity matrix elements or reduced band gaps to nearby states.

Reference

[1] H. Pan, A. M. Ganose, M. Horton, M. Aykol, K. A. Persson, N. E. Zimmermann and A. Jain, Benchmarking coordination number prediction algorithms on inorganic crystal structures, Inorg. Chem. **60**, 1590 (2021).

[2] N. E. Zimmermann and A. Jain, Local structure order parameters and site fingerprints for quantification of coordination environment and crystal structure similarity, RSC Adv. **10**, 6063 (2020).

[3] G. Kresse and J. Furthmüller, Efficiency of ab-initio total energy calculations for metals and semiconductors using a plane-wave basis set, Comput. Mater. Sci. **6**, 15 (1996).

[4] J. P. Perdew, K. Burke and M. Ernzerhof, Generalized gradient approximation made simple, Phys. Rev. Lett. **77**, 3865 (1996).

[5] J. Heyd, G. E. Scuseria and M. Ernzerhof, Hybrid functionals based on a screened Coulomb potential, J. Chem. Phys. **118**, 8207 (2003).

[6] J. Paier, M. Marsman, K. Hummer, G. Kresse, I. C. Gerber and J. G. Ángyán, Screened hybrid density functionals applied to solids, J. Chem. Phys. **124**, 154709 (2006).

[7] D. Sheppard, P. Xiao, W. Chemelewski, D. D. Johnson and G. Henkelman, A generalized solid-state nudged elastic band method, J. Chem. Phys. **136**, 074103 (2012).

[8] A. Togo and I. Tanaka, First principles phonon calculations in materials science, Scr. Mater. **108**, 1 (2015).

[9] R. Nelson, C. Ertural, J. George, V. L. Deringer, G. Hautier and R. Dronskowski, LOBSTER: Local orbital projections, atomic charges, and chemical‐bonding analysis from projector‐augmented‐wave‐based density‐functional theory, J. Comput. Chem. **41**, 1931 (2020).

[10] L. G. Ferreira, M. Marques and L. K. Teles, Slater half-occupation technique revisited: the LDA-1/2 and GGA-1/2 approaches for atomic ionization energies and band gaps in semiconductors, AIP Adv. **1**, 032119 (2011).

[11] M. Brandbyge, J.-L. Mozos, P. Ordejón, J. Taylor and K. Stokbro, Density-functional method for nonequilibrium electron transport, Phys. Rev. B **65**, 165401 (2002).

[12] S. Smidstrup, T. Markussen, P. Vancraeyveld, J. Wellendorff, J. Schneider, T. Gunst, B. Verstichel, D. Stradi, P. A. Khomyakov and U. G. Vej-Hansen, QuantumATK: an integrated platform of electronic and atomic-scale modelling tools, J. Condens. Matter Phys. **32**, 015901 (2019).

[13] H. Tang, B. Shi, Y. Wang, C. Yang, S. Liu, Y. Li, R. Quhe and J. Lu, Layer-Dependent Photoabsorption and Photovoltaic Effects in Two-Dimensional Bi_2O_2X (X= S, Se, and Te), Phys. Rev. Appl. **15**, 064037 (2021).

[14] A. A. Mostofi, J. R. Yates, Y.-S. Lee, I. Souza, D. Vanderbilt and N. Marzari, wannier90: A tool for obtaining maximally-localised Wannier functions, Comput. Phys. Commun. **178**, 685 (2008).